Highlights

Quantitative investigation of internal polarization in a proton exchange membrane water electrolyzer stack using distribution of relaxation times

Jian Zuo, Nadia Yousfi Steiner, Zhongliang Li, Daniel Hissel

- Experimental investigation of a commercialized 1kW PEMWE stack.
- Quantifies the internal polarization processes of the PEMWE using distribution of relaxation times.
- Measures the effect of temperature and cathode pressure on the performance of the PEMWE.
- Compares the contribution of key processes to overall overpotential for the PEMWE and the PEM fuel cell.
- The related experimental datasets are open-sourced.

Quantitative investigation of internal polarization in a proton exchange membrane water electrolyzer stack using distribution of relaxation times

Jian Zuo[a], Nadia Yousfi Steiner[a], Zhongliang Li[a,*], Daniel Hissel[a,b]

[a]*Université Marie et Louis Pasteur, FEMTO-ST, UTBM, CNRS, Belfort, F-90000, France*
[b]*Institut Universitaire de France (IUF), France*

Abstract

Proton exchange membrane water electrolyzer (PEMWE) is a promising technology for hydrogen production due to its ability to operate at high currents, compact design, and high produced hydrogen purity. However, the high cost and limited durability challenges must be addressed to advance the commercialization of PEMWEs. Accessing the internal polarization processes is crucial to understanding the performance of PEMWEs and guiding their design and operation. In practice, the output voltage amplitude on a specific current value is often considered a performance indicator. However, PEMWEs are complex systems with multiple polarization processes that are inaccessible using global indicators such as voltage. We propose a distribution of relaxation times (DRT) based approach to overcome this challenge. DRT is a model-free method that deconvolutes the electrochemical impedance spectroscopy data into a series of relaxation times, corresponding to different internal polarization processes. The results show that the internal polarization processes of the PEMWE can be decomposed into four peaks, corresponding to proton transport in the ionomer of catalyst layer, charge transfer during oxygen evolution reaction and hydrogen evolution reaction, and mass transport. The contribution of these processes and high-frequency resistance (HFR) to the overall overpotential losses are further quantified, which indicates that HFR (79.4%) and charge transfer (16.4%) are the two dominant factors. Finally, the influence of operating temperature and cathode pressure on the performance of the PEMWE is quantified using the proposed approach. This approach can be generalized to identify the degradation root cause of PEMWEs which can guide material enhancement and operation optimization to improve the efficiency and durability of PEMWEs.

Keywords: Proton exchange membrane water electrolyzer, electrochemical impedance spectroscopy, distribution of relaxation times, polarization process, oxygen evolution reaction

1. Introduction

Hydrogen is a promising energy carrier for the future energy system due to its high energy density and pollution-free characteristics during its conversion [1]. Proton exchange membrane water electrolyzes (PEMWEs) operate in a reverse process of a proton exchange membrane (PEM) fuel cell, in which electrical energy is converted into chemical energy by splitting water into hydrogen and oxygen [2, 3]. Thanks to the high efficiency, high purity of generated hydrogen, high dynamic range, and ability to operate at high current densities, PEMWEs are regarded as one of the most promising technologies for hydrogen production [4]. Hydrogen production is clean and sustainable when combined with renewable energy sources, such as wind and solar power [5].

The overall reaction in water electrolyzers is the same, but the half-cell electrode reactions vary depending on the type of electrolyzer. The reactions of a PEMWE are as follows:

$$\begin{aligned} &\text{Anode: } 2H_2O\ (l) \rightarrow O_2\ (g) + 4H^+\ (aq) + 4e^- \\ &\text{Cathode: } 4H^+\ (aq) + 4e^- \rightarrow 2H_2\ (g) \end{aligned} \tag{1}$$

*Corresponding author.
Email address: zhongliang.li@univ-fcomte.fr (Zhongliang Li)

The overall reaction is:

$$2H_2O\ (l) \rightarrow 2H_2\ (g) + O_2\ (g) \tag{2}$$

The PEMWE splits water into oxygen and protons through electrochemical oxidation, that is, oxygen evolution reaction (OER) at the anode. At the cathode, the protons are reduced into hydrogen gas, namely the hydrogen evolution reaction (HER). The protons are transported through the PEM from the anode to the cathode, and the electrons are transported through the external circuit.

Albeit being a promising technology, the development of PEMWEs is still facing challenges, such as high cost, low energy efficiency, and limited durability [6, 7]. Understanding the influence factors of PEMWE's performance is indispensable for overcoming these challenges [8]. Due to the complex structure and multiple internal polarization processes, it has been difficult to fully understand the influence factors of PEMWEs' performance [9].

Works have been done to investigate the influence of operating parameters on the performance of PEMWEs. In general, the operating temperature, pressure, and water flow rate are the three most crucial parameters that influence the performance of PEMWEs [10, 11]. Bazarah et al. [10] categorized these as dynamic factors that can be optimized during operation to enhance the electrolyzer's performance compared to static factors such as stack design and clamping pressure. Li et al. [12] investigated the effect of temperature and pressure on the performance of a high-temperature PEMWE. The results showed that increasing the temperature at a constant pressure of 0.1 MPa increases the concentration overpotential. Increasing operating pressure can help reduce concentration losses. Those observations are only validated for high-temperature electrolyzers. Selamet et al. [13] studied the influence of temperature, pressure, and water flow rate on the performance of a PEMWE. Through the measured polarization curves, they identified that the operating temperature is the most influential factor in the performance. The performance is improved with increasing temperature. The temperature also affects the two-phase flow of water and produced gas inside the PEMWE [10]. Increased temperature enhances bubble transport and reduces bubble accumulation, which can improve performance [14]. The influence of pressure on the performance of PEMWE is relatively complicated. A decreased performance is observed with increasing pressure due to gas crossover [15], increased initialization energy (for starting electrolysis process) [10], and increased activation losses [16]. However, the high-frequency resistance shows a pressure dependence, with an optimal value observed at a medium cathode pressure of 5 bar [17]. The enhanced mass transport is reported with increasing cathode pressure [17]. The water flow can affect the operating temperature and bubble removal thus influencing the performance of PEMWE [14].

In the above studies, the characterization of the PEMWE performance is mainly based on the polarization curve with the voltage-current pairs as performance indicators. The measured voltage losses are global performance indicators, which are the result of multiple internal physicochemical processes. Relying solely on the voltage losses is insufficient to quantify the individual contribution of various internal processes.

Electrochemical impedance spectroscopy (EIS) is a noninvasive, partially *in operando* characterization technique that can provide insights into the internal processes of PEMWEs [18, 19, 20]. To measure the EIS, a small AC amplitude perturbation is applied to the PEMWE with a changing frequency, and the impedance response is recorded. Despite being easily measurable, the interpretation of EIS data is challenging due to the complex simultaneous multiphysical processes occurring in the electrochemical reaction. Equivalent circuit model (ECM) is a commonly used approach to reproduce the EIS spectra using electrical components such as resistors, capacitors, and inductors [21]. A simplified ECM with a series connected resistor, inductor, and a component of parallel connected resistor and constant phase element are used to fit the EIS of a PEMWE [22]. Garcia-Navarro et al. [23] developed a modified Randles ECM with a Warburg element to fit the EIS data of a PEMWE. The key ECM parameters such as high-frequency resistance (HFR), mass transport resistance are obtained by fitting the ECM to the EIS data. Franzetti et al. [24] Investigated the modeling of high-frequency inductive loops in the impedance spectrum of PEMWEs using ECM. However, the model construction is not well explained and the optimization of the model parameters can be misleading if not properly initialized. ECM is a model-based method, which requires prior knowledge of the system to determine a suitable model structure. Moreover, there might be multiple equivalent circuits that can fit the EIS data, which makes the ECM fitting ambiguous [25, 26]. The parameter identification of a complex ECM is also challenging, which requires suitable initial values and optimization algorithms to avoid local minima [27].

Distribution of relaxation times (DRT) is a model-free method that can interpret the impedance data without requiring prior knowledge of the electrochemical systems. By transferring the frequency impedance data into time scales, the internal physicochemical processes of the investigated system can be decomposed based on their time

constants [28]. The application of DRT has been reported in lithium-ion batteries (LIBs) and PEM fuel cells. The timescale identification ability of DRT helps to decouple complex kinetic processes in LIBs [29]. DRT is applied to identify the potential degradation mechanisms and state of health estimation in LIBs [30, 31]. In PEM fuel cells, DRT has been applied to separate and quantify the internal polarization processes such as mass transport and charge transfer [32, 33, 34]. It can further support the fault diagnosis and degradation analysis for PEM fuel cells [35, 36, 37]. By contrast, the DRT analysis has been less explored in PEMWEs. Li et al. [38] implemented DRT analysis to a single cell PEMWE. The water/gas transport, OER, HER, and proton transfer processes are identified. This is one of the earliest works on DRT analysis in PEMWEs. Batalla et al. [39] used DRT to investigate the degradation of a single-cell PEMWE. Besides identifying various internal processes, they revealed that the OER kinetics is the main factor contributing to the degradation of the PEMWE. In summary, the EIS characterization carries abundant information to access PEMWEs' performance and its impact factors, however, the interpretation of EIS has not been fully investigated yet.

According to the literature review, the existing research gaps regarding performance characterization-related studies in PEMWEs are as follows:

- The majority of the previous studies such as [12, 15, 17, 20] focus on the performance of the PEMWE at the cell level, and the experimental studies at the stack level are limited.
- Being a promising technique, EIS is not fully applied to the PEMWE compared with polarization curve-based characterization. The interpretation of EIS spectra is challenging due to the complexity of the internal physicochemical processes. The commonly used ECM-based approach needs to be improved due to its ambiguity, complex parameter identification, and lacking physically meaningful interpretation of model parameters.
- Quantitative analysis of the individual contribution of internal polarization processes is missed in the literature. However, it is indispensable to understand the performance-limiting factors in PEMWEs.

By addressing these research gaps, the contributions of this study are as follows:

- Experimental works on PEMWE at the stack level are used to investigate its internal polarization processes.
- Propose a DRT-based approach to quantify the influence of operating temperature and cathode pressure on the performance of the PEMWE stack.
- Conduct a comparative study with PEM fuel cells to give a direct insight into PEMWE EIS. The structural and compositional similarities with PEM fuel cells allow transferring their development into PEMWEs. However, the similarities and differences in internal characteristics between those two technologies must be understood to facilitate the transition. This is addressed in this contribution through EIS analysis.

To sum up, the main novelties of this work include: 1) proposing a DRT-based approach for interpreting the internal polarization processes in PEMWEs, 2) providing a quantitative investigation of the contribution of individual processes to overall overpotential losses, and 3) conducting a comparative study with PEM fuel cells to highlight their differences in EIS characteristics. In the following sections, the experimental setup and materials about the tested PEMWE stack are presented in Section 2. Next, the validation of impedance data and DRT calculation approaches are illustrated in Section 3. Then, the results of DRT analysis and the influence of operating temperature and cathode pressure on the performance of the PEMWE stack are presented in Section 4. Finally, Section 5 provides a summary of the conclusions and outlines potential directions of future work.

2. Experimental

PEMWE stack. A commercial 1kW PEMWEstack is used for the performance characterization. The stack is composed of 10 cells, with a cell area of 25 cm^2. Detailed physical parameters of the tested electrolyzer stack are shown in Table 1.

Table 1: General physical parameters of the tested PEMWE stack.

Parameters	Value	Unit
Nominal load	1	kW
Number of cells	10	
Cell area	25	cm^2
H_2 maximal production	225	$Nl.h^{-1}$
Operating temperature	30-70	°C
Operating pressure H_2	0-20	bar
Operating pressure O_2	1 (unpressurized)	atm
Stack dimensions	85×85×150	mm
Weight	2.5	kg

Performed tests. The PEMWE stack is tested under different temperatures and pressures (only the cathode is pressurized, and the anode side is maintained at atmospheric pressure) to measure its performance. Specifically, the sequential test protocols performed for the new stack are listed as follows:

1) Activation test: operate the stack at 30 A for 8 hours.
2) Test1: set the operating temperature to 60 $^{\circ}C$, and the cathode pressure is 1 bar.
3) Test2: set the operating temperature to 60 $^{\circ}C$, and the cathode pressure is 5 bar.
4) Test 3-5: set the cathode pressure to 3 bar, and control the operating temperature to 40 $^{\circ}C$, 50 $^{\circ}C$, and 60 $^{\circ}C$, respectively.

The values of the operational parameters are set based on reference values listed in Table 1. The operating temperature is suggested to be in the range of 30-70 °C. Thereby, we have selected three temperature points, namely 40, 50, and 60 °C, for the test. The cathode pressure is suggested to lie below 20 bar. We selected the pressure of 1, 3, and 5 bars for conducting the test. Since a homemade test bench is used rather than a commercial one, we did not select too high pressure for safety considerations. It is noticed that the operating temperature and pressure are selected as the investigated operating parameters since these are the most influential performance-limiting factors as indicated in the literature. The physical configuration of the test bench and auxiliary systems are depicted in Fig. 1.

Characterization tests. For each test scenario (tests 1 to 5), the polarization curve and EIS characterizations are measured. The polarization curve is measured by ramping the current density from 0 to 2 $A.cm^{-2}$ in 8,000 seconds, and the voltage is recorded at each current density. Complete or partial EIS is measured at DC currents of 5, 10, 15, 20, 25, 31.25, 37.5, 43.75, and 50 A, respectively. Two types of frequency ranges are employed during the EIS test. The frequency range is from 0.05 Hz to 5 kHz (full frequency range) for DC currents of 15, 25, 37.5, and 50 A, and from 5 Hz to 16 kHz (without low-frequency data) for DC currents of 5, 10, 20, 31.25, and 43.75 A. Omitting the low-frequency range for part of the DC currents is only for saving the measuring time. The AC amplitude disturbance is set to 10% of the DC amplitude.

3. Methodology

3.1. Analysis of electrochemical impedance spectroscopy spectrum

Characteristics of EIS spectra. A typical EIS spectrum of a PEMWE is shown in Fig. 2. Similar to the discussion of impedance spectrum in PEM fuel cells [40], the spectrum in PEMWEs can be classified into five regions:

- (extreme) Low-frequency inductive loop. The inductive loop appears at the extreme low-frequency range of an EIS spectrum. The actual causes of this inductive loop are still unclear due to limited literature.
- Low-frequency mass transport region. The low-frequency resistive region is related to the mass transport of reactants (water) and gas products (hydrogen and oxygen) in the PEMWE (process 1).

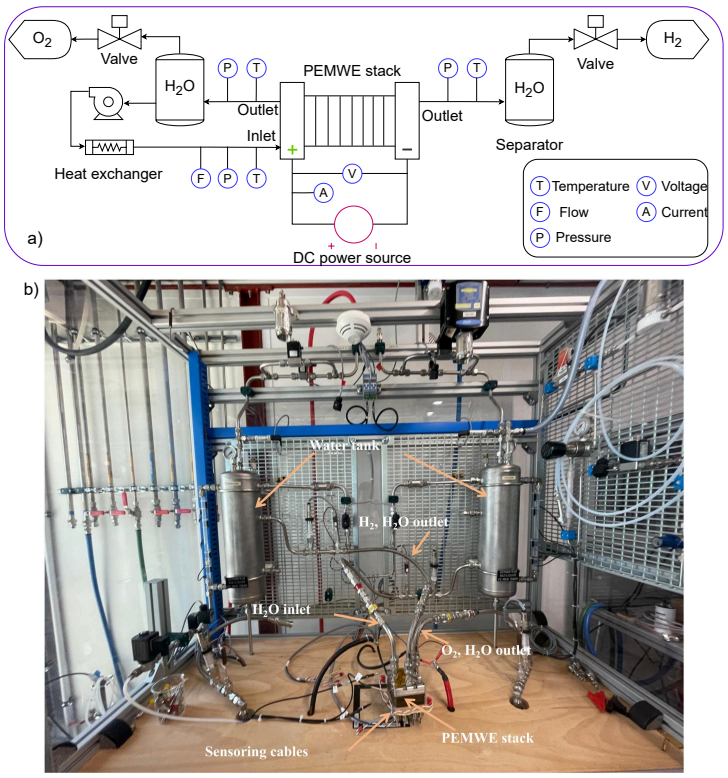

Figure 1: Configuration of the PEMWE test bench. a) Schematic diagram of the test bench and b) physical configuration of the test bench.

- Middle-frequency charge transfer region. This region is related to the charge transfer kinetics of the OER and HER reactions (process 2). Note that the OER is the rate-limiting step in the PEMWE.
- High-frequency proton transfer region. The high-frequency region is associated with the proton transport in the ionomer of the catalyst layer (process 3).
- (extreme) High-frequency inductive region. An inductive loop is observed at the extreme high-frequency range, which is related to the measurement equipment and load cables.

Processes 1, 2, and 3 are the internal polarization processes of the PEMWE, which are closely linked to its performance and will be further investigated in the following sections. The total polarization resistance is the sum of the resistances of these processes, as shown in Fig. 2. The intercept of the EIS with the real axis at the high-frequency range is called the high-frequency resistance (also known as ohmic resistance). HFR is the sum of the ohmic resistance of PEM (dominant), current collectors, and contact resistance.

Validation of impedance data. To ensure that the measured impedance spectra are suitable for the following analysis, all impedance data are validated to meet the linearity, stability, and causality requirements [28, 36]. A standard validation process is used based on the Kramers-Kronig (KK) relation [41]. This KK-relation links the real and imaginary parts of an impedance spectrum. The validity of the spectrum is checked using a KK-compliant ECM, which writes:

$$Z_{\mathrm{KK}}(\omega) = R_{ohm} + \sum_{i=1}^{m} \frac{R_i}{1 + j\omega\tau_i} \tag{3}$$

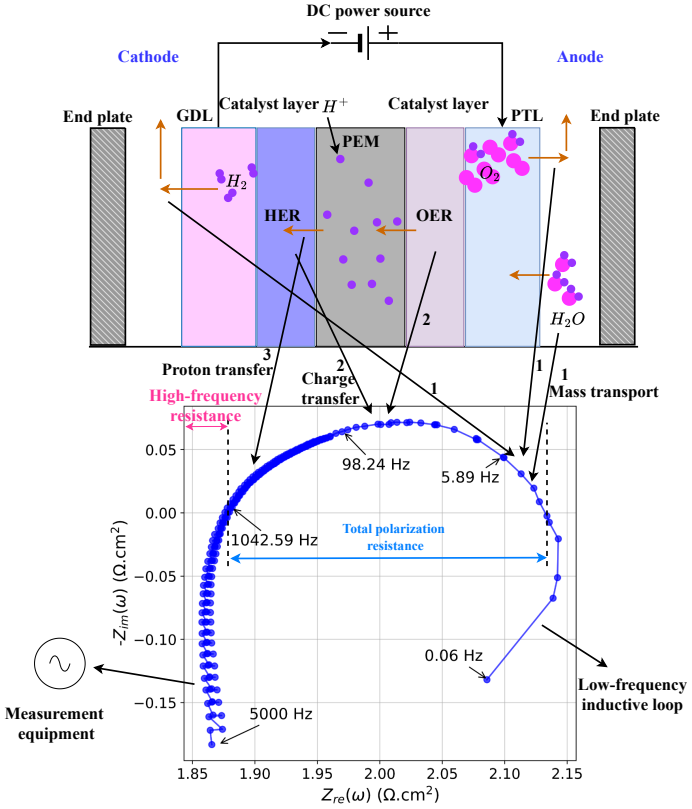

Figure 2: Typical EIS spectrum and related processes of a PEMWE. PTL: porous transport layer, GDL: gas diffusion layer, OER: oxygen evolution reaction, HER: hydrogen evolution reaction.

where $\tau_i = R_i C_i$ stands for the time constant of the i-th R//C circuit. j is the imaginary unit. The optimal number of R//C circuits is decided by introducing a ratio criterion β, which writes [41]:

$$\beta = 1 - \frac{\sum_{R_i<0} |R_i|}{\sum_{R_i>0} |R_i|}. \tag{4}$$

Then m is gradually increased within a maximum limit until $\beta < c$ is reached ($c = 0.24$ is used) [36]. Then, the KK residuals can be computed by:

$$\begin{aligned} \Delta Z_{re} &= \frac{Z_{re}(\omega) - \hat{Z}_{re}(\omega)}{|Z(\omega)|} \\ \Delta Z_{im} &= \frac{Z_{im}(\omega) - \hat{Z}_{im}(\omega)}{|Z(\omega)|} \end{aligned} \tag{5}$$

where $Z_{re}(\omega)$, $Z_{im}(\omega)$, and $Z(\omega)$ represent the real, imaginary parts and complex impedance of the EIS data. $\hat{Z}_{re}(\omega)$ and $\hat{Z}_{im}(\omega)$ are the real and imaginary parts of the estimated impedance obtained using the KK-compliant equivalent circuit. The measured spectrum is considered to be validated when the computed KK residuals are smaller than 1%.

3.2. Distribution of relaxation times-based deconvolution

The key idea of DRT analysis is to transform frequency domain EIS data into time domain by applying a larger number of serially connected R//C components (the single component is composed of parallel connected resistor and capacitor). The DRT $h(\tau)$ is related to the measured impedance data by the following equation [28]:

$$Z(\omega) = R_0 + j\omega L_0 + \int_0^{\infty} \frac{h(\tau)}{1 + j\omega\tau} d\tau \tag{6}$$

where R_0 stands for the ohmic resistance, f is the frequency, and $\omega = 2\pi f$ represents the angular frequency. $\tau = RC$ is the time constant of the R//C circuit. L_0 stands for the inductance. This inductive behavior is mostly caused by the connecting cables between the impedance spectrometer and the PEMWE.

Eq. (6) is further transferred into logarithmic form using $u = \ln(\tau)$, which writes:

$$\begin{aligned} Z(\omega) &= R_0 + j\omega L_0 + \int_{-\infty}^{\infty} \frac{\gamma(\tau)}{1 + j\omega\tau} d\ln(\tau) \\ &= R_0 + j\omega L_0 + R_p \int_{-\infty}^{\infty} \frac{g(\tau)}{1 + j\omega\tau} d\ln(\tau) \end{aligned} \tag{7}$$

where $\gamma(\tau) = \tau h(\tau)$, $g(\tau)$ is the normalized distribution. The polarization resistance R_p is computed by the area under the DRT peaks, which is expressed as:

$$R_p = \int_{\tau_l}^{\tau_u} \gamma(\ln(\tau)) d\ln(\tau) \tag{8}$$

where τ_l and τ_u are the lower and upper limits of the decomposed DRT peaks. The time constant of the decomposed peak is associated with a specific polarization process in the studied electrochemical system.

The calculation of DRT from Eq. (7) constitutes an ill-posed problem. Consequently, numerical solutions employing various regularization techniques are used. The Tikhonov regularization and radial basis function with prior data screening and weight assigning are used in this work. This enhances the robustness of DRT calculation to noisy EIS spectra. The calculation is achieved thanks to the open-source software, *EISart* [42]. In Tikhonov regularization, a penalty term is weighted by the regularization parameter λ and the optimization problem is formulated as [43]:

$$\min_x J_x = ||Ax - b||^2 + ||\Gamma x||^2 \tag{9}$$

where $x \in \mathbf{R}^{N_\tau}$ is the parameters used to compose the function $\gamma(\tau)$, N_τ is a hyperparameter for deciding the dimension of x. $||Ax-b||^2 = \sum_{i=1}^{N_f} err_{Re,i}^2(\tau) + \sum_{i=1}^{N_f} err_{Im,i}^2(\tau)$, the error of real part is $err_{Re} = Re(Z_{mes}) - Re(Z_{DRT})$, and error of imaginary part is $err_{Im} = Im(Z_{mes}) - Im(Z_{DRT})$. b is the matrix composed of real and imaginary parts of the impedance spectrum,

Table 2: Comparison of DRT and ECM in terms of EIS interpretation

	DRT	ECM
Prior knowledge	Model-free	Model-based
Data domain	Timescale	Frequency
Interpretability	Physical-meaningful peak assignment	No guarantee on physical meaning
Optimization methods	Tikhonov regularization, maximum entropy, Fourier transform, Gaussian process, Genetic algorithms, Monte Carlo deconvolution Bayesian optimization, deep neural networks	Complex nonlinear least squares
Complexity	Flexible, coherent, and nonparametric	Complicated with complex circuits
Extensibility	Well-developed for various applications	Limited to a specific application
Pitfalls	Sensitive to noise, pseudo peaks	Ambiguity and above

namely $b = \begin{bmatrix} Re(Z_{mes}) \\ Im(Z_{mes}) \end{bmatrix}$. A is the matrix to be calculated for the measured frequencies and predefined time constants, which writes:

$$A = \begin{bmatrix} Re(\frac{1}{1+j\omega_1\tau_1}), & \cdots, & Re(\frac{1}{1+j\omega_1\tau_{N_\tau}}) \\ \vdots, & \vdots, & \vdots \\ Re(\frac{1}{1+j\omega_{N_f}\tau_1}), & \cdots, & Re(\frac{1}{1+j\omega_{N_f}\tau_{N_\tau}}) \\ Im(\frac{1}{1+j\omega_1\tau_1}), & \cdots, & Im(\frac{1}{1+j\omega_1\tau_{N_\tau}}) \\ \vdots, & \vdots, & \vdots \\ Im(\frac{1}{1+j\omega_{N_f}\tau_1}), & \cdots, & Im(\frac{1}{1+j\omega_{N_f}\tau_{N_\tau}}) \end{bmatrix}.$$

$\Gamma = \lambda I$ is the penalty term, and I the identity matrix. The regularization parameter λ determines both the smoothness and resolution of the DRT results. N_f is the number of measured data points in the EIS spectrum. $\lambda = 1 \times 10^{-3}$ is found to give a good tradeoff for the measured EIS. In *EISart*, the polarization resistance R_p is refined with a series of parallel-connected resistance and constance phase element-based ECM to obtain the final results [42].

Comparison with equivalent circuit model. Additional justification for the choice of DRT over ECM is provided here. A summary of the comparisons of the two approaches over aspects such as prior knowledge and data domain are given in Table 2. DRT is a model-free approach while ECM is a model-based approach that requires prior knowledge of the investigated electrochemical system. ECM directly uses the frequency impedance data for identifying the circuit model, while DRT transfers the impedance data from the frequency domain to the timescale, providing useful insights into the internal dynamic processes of the studied system. The EIS deconvolution using DRT usually provides physical-meaningful interpretations of the identified peaks, while the parameters optimized from ECM can be physically meaningless. For example, Giner-Sanz et al. [44] investigated twelve different circuits to identify a physically meaningful ECM.

DRT has received a growing research interest with numerous optimization methods being proposed such as Tikonov optimization, Gaussian process, and deep neural networks. The parameter optimization of an ECM mainly relies on complex nonlinear least squares. As the complexity of the circuit increases, the parameter optimization becomes increasingly complicated. DRT is a flexible, coherent, and nonparametric approach that allows deconvoluting EIS in a unified setting and offers a unique visual interpretation [45]. DRT is a flexible and extensible approach that adapts for performance characterization, fault diagnosis, and degradation analysis in various electrochemical systems. It can be further combined with ECM for peak quantification and assignment. Ambiguity, namely multiple circuits might produce the same spectrum, is another well-known pitfall of ECM. However, due to the high resolution of DRT, a small noise or error in the impedance spectrum could lead to a large deviation in DRT, resulting in misunderstanding interpretations. Another issue is the pseudo peaks calculated during DRT deconvolution. However, these issues can be avoided by providing high-quality EIS data and proper parametrization of DRT optimization methods.

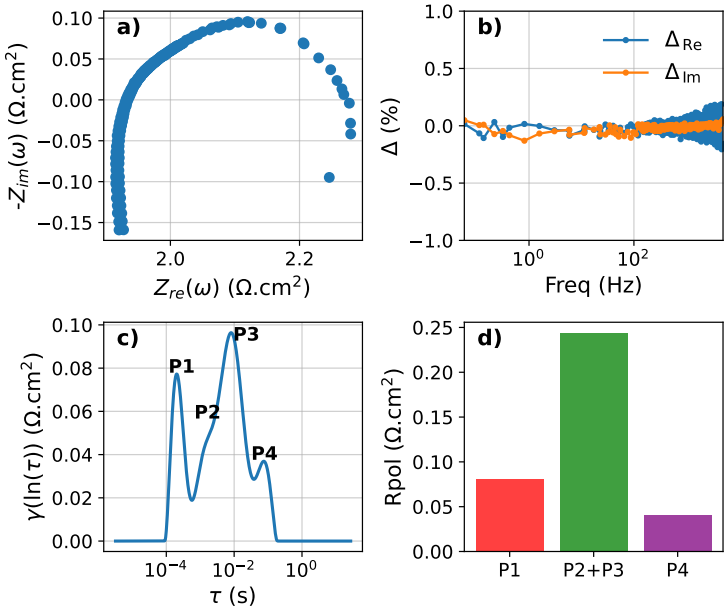

Figure 3: The DRT results of the studied PEMWE at 40 $^{\circ}C$ and 3 bar (DC current of 1.5 A.cm^{-2}). a) Nyquist plot, b) Lin-KK test results, c) the decomposed DRT curve with identified peaks, and d) polarization resistances of the identified processes.

4. Results and discussion

First, the DRT analysis results will be presented to show the decomposed peaks of the internal polarization processes, including proton transfer in the ionomer, charge transfer during OER and HER, and mass transport. Based on the EIS spectra obtained under different DC currents, those decomposed peaks are assigned to specific internal polarization processes to quantify their contribution to overall polarization losses. Finally, the operating temperature and cathode pressure alter the internal polarization processes, thus influencing the performance of the PEMWE. This will be further checked by combining the polarization curve and EIS analysis.

4.1. Distribution of relaxation times analysis

Decomposed peaks. The EIS spectrum validation and DRT analysis can be achieved by applying the deconvolution strategy demonstrated in Section 3. As an example, the EIS spectra measured at 40 $^{\circ}C$ and 3 bar (DC current of 1.5 A.cm^{-2}) are shown in Fig. 3a). The Lin-KK test error results of the real (Δ_{Re}) and imaginary (Δ_{Im}) parts of the impedance spectra are shown in Fig. 3b). The relative errors are below 0.5%, which indicates that the EIS spectra are valid for the subsequent DRT analysis. In the DRT analysis, four peaks are identified from the EIS spectrum, as shown in Fig. 3c). Since peak 2 (P2) overlaps with peak 3 (P3), the polarization resistance (R_{pol}) of P2 and P3 are calculated together as shown in Fig. 3d). The resistance of charge transfer during OER and HER is the largest among the identified processes. Note that the influence of the DC power source on the obtained impedance is minimized by preventing the excitation signal pass through it. Moreover, the inductance and pseudo inductance are considered during the DRT calculation which could also help to ensure the deconvolution accuracy [42]

Interpretation of DRT peaks. To assign the decomposed peaks to the internal polarization processes, the DRT results are computed at different DC currents. Fig. 4 shows the DRT results of the studied PEMWE operated at 40$^{\circ}C$ and 3 bar. Figs. 4a), b) are the Nyquist plot of the measured EIS spectra. The spectra of 15, 25, 37.5, and 50A are measured with a full frequency range (0.05 Hz-5 kHz), while the spectra of 5, 10, 20, 31.25, and 43.75 A are measured with a frequency range of 5 Hz-16 kHz. The computed DRT results are shown in Fig. 4c), d), respectively. Four individual peaks are identified, P1, P2, P3, and P4 as shown in Fig. 4c). P4 is missing in Fig. 4d) due to the limitation of the frequency range (missing low-frequency measurements). Besides, it should be noted that P3 may not be a complete peak due to the frequency range limitation.

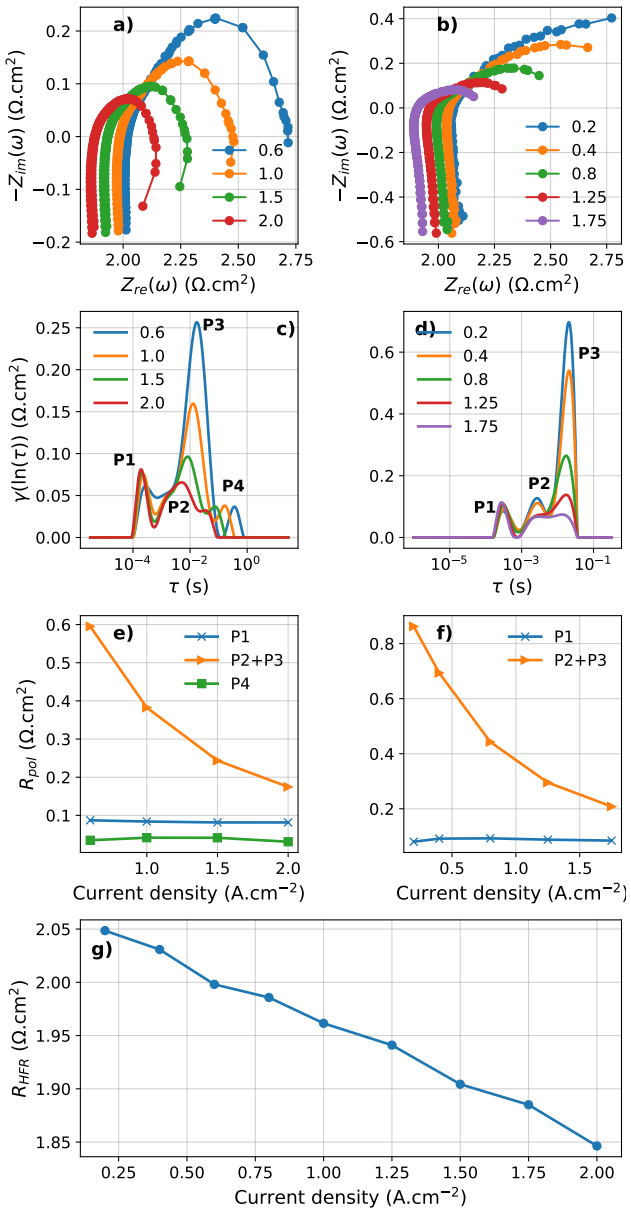

Figure 4: The DRT results of the studied PEMWE at 40 $°C$ and 3 bar. a), b) The measured EIS spectra, c), d) the deconvoluted DRT peaks of the EIS spectra, e), f) the computed polarization resistances, g) the computed high-frequency resistances. The unit of legend in a), b), c), and d) is $A.cm^{-2}$.

Table 3: Assigned polarization processes, the corresponding time constants, and the frequency range.

Peak	Assigned process	Time constant (s)	Frequency range (Hz)
P1	Proton (H^+) transport inside ionomer	2.29×10^{-4}(I = 1 A.cm^{-2})	200-2,000
P2	Charge tranfer of HER		30-230
P3	Charge tranfer of OER	1.28×10^{-2}(I = 1 A.cm^{-2})	1.5-280
P4	Mass (H_2O, gas) transport	7.46×10^{-2}(I = 1 A.cm^{-2})	0.2-7

A similar variation trend of the identified peaks over DC currents is observed in Fig. 4c) and d). P1 is nearly constant with increasing DC current, which is assigned to the proton transport inside the anode and cathode ionomer. Both P2 and P3 are shrinking with increasing DC current, while the area under P3 is much larger compared to P2. Thus, P2 is assigned to the charge transfer during HER, and P3 is assigned to the charge transfer during OER (the dominant one). This is consistent with the fact that the OER is more sluggish than the HER. P4 is assigned to the mass transport of water and gas (hydrogen and oxygen), which is observed at the highest τ. Table 3 summarizes the assigned polarization processes as well as the time constants and frequency ranges. At 1 A.cm^{-2}, the time constants of the identified processes are: P1: 2.29×10^{-4} s, P2 and P3 (overlapped peaks): 1.28×10^{-2} s, P4: 7.46×10^{-2} s. The time constants of P2 (individual peak) at 0.8 A.cm^{-2} is 1.7×10^{-2} s. According to the obtained DRT results, the general frequency range of the identified processes is: P1: 200-2,000 Hz, P2: 30-230 Hz, P3: 1.5-280 Hz, P4: 0.2-7 Hz.

To quantify the contribution of each polarization process to the overall polarization losses, the polarization resistances of the identified processes are calculated using Eq. (8). The results are shown in Fig. 4e), f). It can be seen that the charge transfer resistance R_{ct} (P2 and P3) is the dominant polarization process, followed by the ionic transport resistance R_{pt} (P1), and mass transport resistance R_{mt} (P4). The R_{ct} is decreasing sharply with increasing DC current, while the R_{pt} and R_{mt} are nearly constant. Note that the mass transport resistance only shows a slight increase with increasing DC current, which indicates that the tested PEMWE is well fabricated and shows high performance even under high current load. Moreover, the active area of the tested PEMWE is relatively small (25 cm^2) which may not be critical for detecting obvious bubble removal issues. An obvious decreasing trend is observed for HFR as shown in Fig. 4d). This observation further verifies that the PEMWE is maintained at well-hydrated states even when operating at relatively high currents. The mass transport is maintained at a relatively low level which proves the good mass transport capabilities under the tested currents.

Contribution of individual processes to overall overpotential losses. Based on the computed polarization resistances, the contribution of each internal polarization process to the overall overpotential losses can be computed as [46]:

$$\eta_{\text{ps}}(I) = \int_{I_l}^{I_u} R_{ps}(I)dI = \sum_{I_l}^{I_u} R_{ps}(I_n)\Delta I_n \tag{10}$$

where I_l and I_u represent the lower and upper limits of the DC current, respectively. R_{ps} is the polarization resistance of the identified process, and ΔI_n is the discretized current step, the smaller the step, the more accurate the estimated losses. This formula is generic to calculating overpotential from the estimated polarization resistances.

Then the overpotentials of DC currents from 0.2 to 2 A.cm^{-2} of the identified processes at 2 A.cm^{-2} are calculated based on Eq. (10):

- Proton transport resistance R_{pt}: 0.15 V, contributes 3.5% to the overall overpotential losses,
- Charge transfer resistance R_{ct}: 0.73 V, contributes 16.4% to the overall overpotential losses,
- Mass transport resistance R_{mt}: 0.03 V, contributes 0.7% to the overall overpotential losses,
- High-frequency resistance R_{HFR}: 3.51 V, contributes 79.4% to the overall overpotential losses.

Due to the difficulties in obtaining the impedance under open circuit voltage conditions, the lowest current density for measuring the EIS is set as 0.2 A.cm^{-2}. The results indicate that the HFR and charge transfer process are the dominant factors for determining the overall performance of the PEMWE.

Comparison with PEM fuel cells. A typical DRT analysis results of a PEM fuel cell, as shown in Fig. 5 is used to compare with the results of the PEMWE [47, 48]. The cell area of the tested PEMWE stack and PEM fuel cell are both 25 cm^2. Table A.1 lists the main physical parameters of the PEM fuel cell. The processes of the identified peaks in the PEM fuel cell are summarized as follows:

- k1: Electrode and membrane contact effects,
- k2: Proton transport in the cathode ionomer,
- k3: Charge transfer during hydrogen oxidation reaction,
- k4: Charge transfer during oxygen reduction reaction,
- k5: Mass transport of oxygen.

In PEM fuel cell, the time constants of peaks k2, k4, and k5 at 1 $A.cm^{-2}$ are 1.95×10^{-4}, 4.93×10^{-3}, and 4.0×10^{-2} s, respectively. It is found that the time constant of the charge transfer process in PEMWE (1.28×10^{-2}) is much larger than that of the PEM fuel cell. The mass transport process in PEMWE (7.46×10^{-2}) is also larger than that of the PEM fuel cell. The proton transport process of PEMWE and PEM fuel cell are similar. These observations indicate that the OER and HER processes in PEMWE are more sluggish than those of the PEM fuel cell. As for the time constant of the mass transport process, the mass transport in PEMWEs involves the transport of reactant water, while in PEM fuel cells it is reactant gases, thus a larger time constant is observed in PEMWEs.

Another difference is the characteristics of the mass transport process. The mass transport resistance of the PEM fuel cell increases sharply with increasing DC current as observed in Fig. 5d). While the mass transport resistance of PEMWE tends to remain relatively low and shows non-monotonic variation. The reason why the mass transport resistance of the PEMWE is relatively small could be linked to the flow field design. The design could be optimized to facilitate the easy transfer of water and reactants to the reaction site, especially in a commercial PEMWE stack. The non-monotonic variation behavior in PEMWE's mass transport resistance may linked to PEMWE's internal reaction characteristics such as bubble removal. Moreover, it is found that the useful frequency range of PEMWE (around 0.2 Hz) is relatively higher than that of the PEM fuel cell (usually needs to be measured at the lowest frequency of 0.01 Hz). This implies that a fast EIS characterization is possible for PEMWEs by limiting the low-frequency limits.

Both the PEM fuel cell and PEMWE show a decreasing trend of the high-frequency resistance with increasing DC current. However, the HFR of PEMWE is much larger than that of the PEM fuel (0.048 $\Omega.cm^2$ per cell for PEM fuel cell and 0.196 $\Omega.cm^2$ per cell for PEMWE at 1 $A.cm^{-2}$). This implies that the HFR of PEMWE is a dominant factor for determining the overall performance of the PEMWE.

The difference in the contribution of individual processes to the overall overpotential losses of the PEMWE and PEM fuel cell is shown in Fig. 6. It verifies that the HFR and charge transfer processes are the dominant factors for determining the overall performance of the PEMWE, while the mass transport and charge transfer processes are the dominant factors for determining the overall performance of the PEM fuel cell. It is noted that the comparison results concluded here reflect the intrinsic characteristic differences between PEMWEs and PEM fuel cells. This will not be changed by other factors such as the number of cells. For instance, in [36], we have found that the charge transfer mass transport processes are the two dominant factors for PEM fuel cell performance degradation. The two investigated stacks are fabricated with 10 cells, the same as the tested PEMWE stack.

4.2. Influence of temperature

The temperature influences all the internal physicochemical processes that take place inside a PEMWE. Overall, the performance is enhanced with the increase in temperature, as observed in the polarization curve (Fig. 7).

DRT analysis is performed on the measured EIS spectra at different temperatures, and a group of Nyquist curves measured for DC current of 25 A is shown in Fig. 7b). Specifically, the polarization processes of EIS spectra measured at DC currents of 15, 25, 37.5, and 50 A, namely 0.6, 1.0, 1.5, and 2.0 $A.cm^{-2}$, are decomposed. The calculated polarization resistances of each process are compared to quantify the influence of temperature on the internal polarization processes. Fig. 7c) presents the results of the proton transport resistance R_{pt}. It shows that for all current loads, the proton transport resistance decreases with increasing temperature, except for 50 °C at 15 A. The measurement error might cause this. The proton conductivity is enhanced with increasing temperature, thus

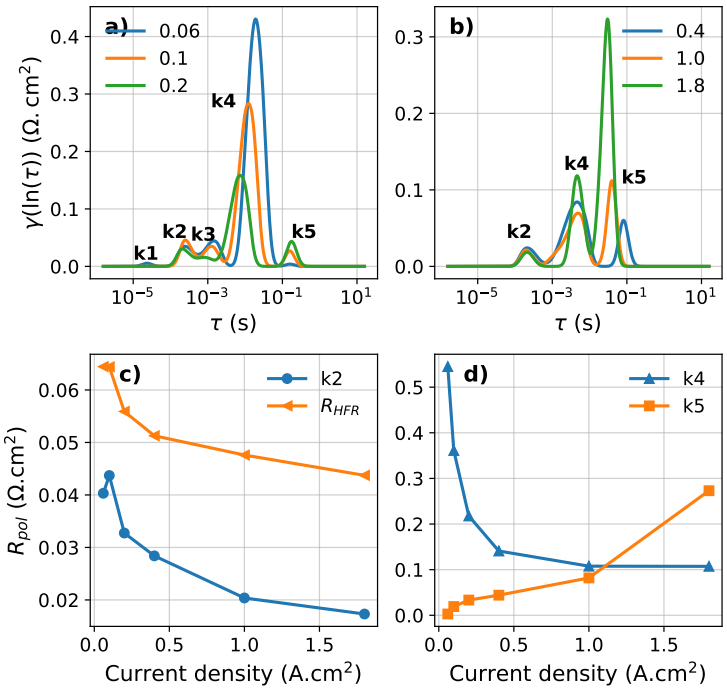

Figure 5: The DRT results of a typical PEM fuel cell (single cell, with data from [47]). a) The decomposed DRT peaks of EIS spectra measured at 0.06, 0.1, and 0.2 A.cm^{-2}, b) the decomposed DRT peaks of EIS spectra measured at 0.4, 1.0, and 1.8 A.cm^{-2}, c) the calculated polarization resistance of hydrogen oxidation reaction and high-frequency resistance, d) the calculated polarization resistances of oxygen reduction reaction and mass transport processes.

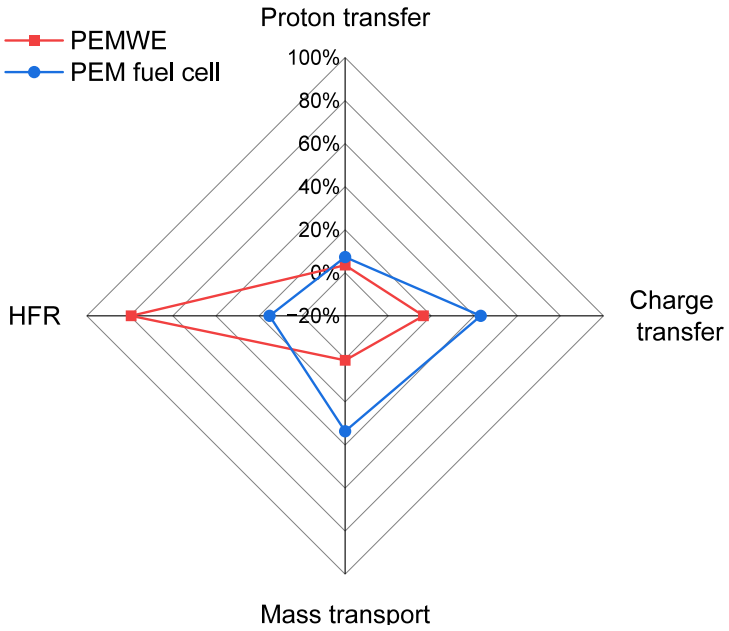

Figure 6: Comparison of the contribution of key processes to overall overpotential losses for the PEMWE and the PEM fuel cell.

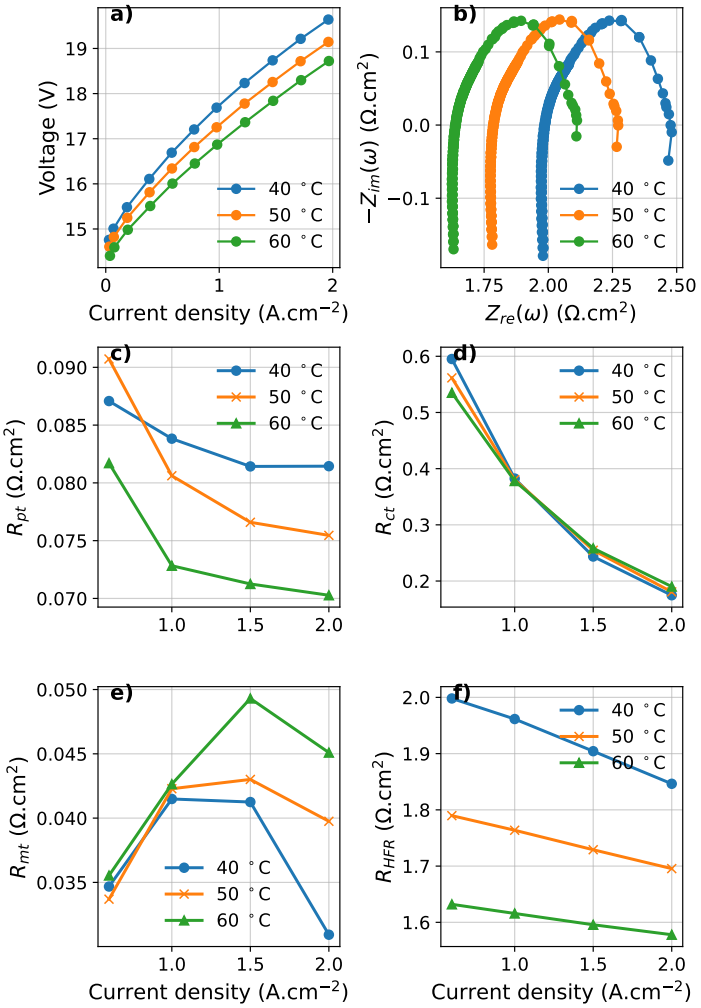

Figure 7: Influence of temperature on the performance of the studied PEMWE. a) Polarization curves measured at 40, 50, and 60 °C, b) EIS spectra at $I = 1$ A.cm^{-2}, namely 25 A, c) proton transport resistances R_{pt} under different temperatures, d) charge transport resistances R_{ct} under different temperatures, e) mass transport resistances R_{mt} under different temperature, f) high-frequency resistances HFR under different temperature.

a decreasing trend is observed for R_{pt}. The high-frequency resistance R_{HFR} also shows a decreasing trend with increasing temperature, as shown in Fig. 7f). As seen in the figure, the value as well as the variation of R_{HFR} is the largest among all the resistances, which is the dominant factor for determining the overall performance of the PEMWE. The increase in conductivity of all cell components with increasing temperature is the main reason for the decrease in R_{HFR}. In [49], the authors attribute the effects of high temperature to the easy transport of species, higher exchange current density, and conductivity, which are consistent with the above analysis. Kang et al. [50] reported a similar variation in R_{HFR} under elevated temperature using a Randles circuit model. However, the ECM-based approach is less flexible and accurate compared with the DRT-based approach. For example, only a total charge transfer resistance is obtained without distinguishing the anode and cathode. Another interesting observation is that the R_{HFR} shows a decreasing trend with increased DC currents. This is supposed to be caused by the accumulated heat generation under high currents which increase the internal temperature. As a result, the electron and proton conductivity was improved.

In comparison to the results of R_{pt} and R_{HFR}, the charge transport resistance R_{ct} and mass transport resistance R_{mt} show less significant changes with increasing temperature. In general, the R_{ct} shows a slight decrease with increasing temperature which implies that the OER and HER processes are enhanced at higher temperatures. However, this improvement is not as significant as R_{pt} and R_{HFR} in the investigated temperature range. It is surprising that R_{mt} shows a slight increase with increasing temperature under high currents (Fig. 7). We speculate that this is due to the increased inductive loop under high currents and lower temperature as observed in Fig. 7e). This is supported by a recently published study [51]. However, as the mass transport resistance is relatively small compared to the other resistances, thus, the influence of temperature on R_{mt} is less significant.

4.3. Influence of cathode pressure

The results of the influence of cathode operating pressure on the performance of the PEMWE are shown in Fig. 8. In general, the performances are relatively close under the investigated scenarios according to Fig. 8a). In the initial current range, the performance of the PEMWE decreases with increased pressure. But for the high current range (above 40 A), the voltage of 3 bar and 5 bar are below that of 1 bar. The water electrolysis process shifts from mass transport limited to energy-limited due to the free energy change associated with water dissociation as a function of pressure and temperature [10]. The higher the pressure, the higher the input energy required to initiate the water electrolysis process. According to the experimental data, the electrolysis process starts at approximately 14.2, 14.4, and 14.5 V for PEMWE stack under 1, 3, and 5 bar, respectively. Thus, in the initial stage, the performance of the PEMWE decreases with increasing pressure. A similar conclusion is given in [52].

The variation of proton transfer resistance R_{pt} under different cathode pressures and currents is illustrated in Fig. 8c). For all DC currents, it is observed that R_{pt} decreases with increasing cathode pressure. This implies an enhancement of proton transport with increasing cathode pressure. This may caused by improving contact between components of the PEMWE stack such as the membrane and cathode catalyst layer which facilitates the proton transfer. Moreover, a relatively large variation in R_{pt} is observed at relatively low currents, namely 0.6 and 1.0 A.cm^{-2}. It is seen from Fig. 8d) that the charge transfer resistance R_{ct} is decreasing with increasing pressure. This indicates that the OER and HER processes are enhanced at higher pressures. Regarding the variation versus increasing pressure, R_{mt} follows the same trend as shown in Fig. 8e). The positive influence of increased pressure on mass transport losses is also reported in [17, 53]. However, it is observed that R_{mt} shows a relatively large decrease when pressure increases from 1 to 3 bar. The decrease in R_{mt} is relatively lower when pressure increases from 3 to 5 bar. This reflects the complex relationship between bubble removal and cathode pressure. More pressure points may need to be tested to fully understand their influence on the mass transport process. Regarding the variation versus currents, R_{mt} increases with increasing currents at 1 bar. However, when further increasing the cathode pressure, a non-monotonic variation trend is observed, with the largest R_{mt} observed at 1.5 A.cm^{-2}. One interesting observation is that there is a relatively larger decrease in R_{mt} at 3 bar and 5 bar compared to that of 1 bar when operating under high current loads. This is linked to the performance shift for 3 bar and 5 bar as discussed in Fig. 8a). The HFR results are shown in Fig. 8f). It shows that the influence of pressure on the HFR is not monotonic. The HFR of 3 bar and 5 bar are below that of 1 bar. However, the HFR of 5 bar is higher than that of 3 bar. More investigations are needed to understand the influence of pressure on the HFR. The non-monotonic behavior of the HFR with increasing pressure is also reported in [17].

To sum up, the influence of increasing pressure on the performance of the PEMWE is not straightforward. In the lower and middle current range (initial stage), the performance of the PEMWE slightly decreases with increasing pressure. However, due to the enhanced internal polarization processes at higher currents with the increase of pressure,

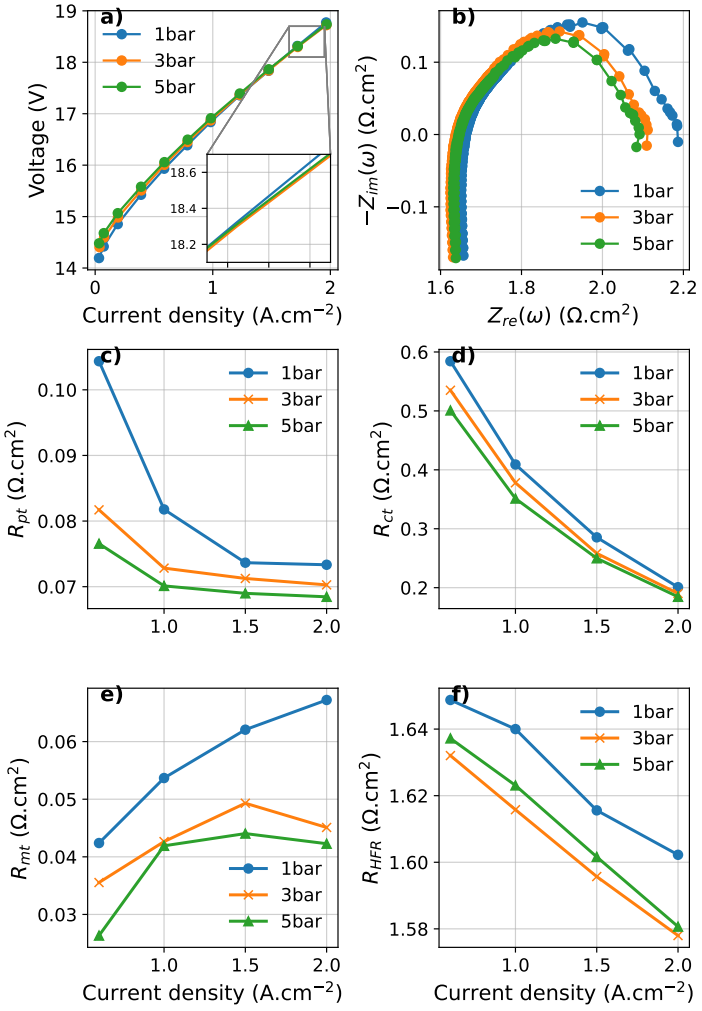

Figure 8: The influence of pressure on the performance of the studied PEMWE. a) Polarization curve, b) EIS spectra at I = 25 A (1 A.cm^{-2}), c) proton transport resistances R_{pt} under different pressures, d) charge transport resistances R_{ct} under different pressures, e) mass transport resistances R_{mt} under different pressures, f) high-frequency resistances HFR under different pressures.

the performance of the PEMWE at 3 bar and 5 bar is better than that of 1 bar. More comprehensive experiments with a wider pressure range may needed to draw a clearer conclusion.

5. Conclusion

This study investigates the PEMWE performance evaluation methods by using the DRT method. The performance of a commercialized 1kW PEMWE stack under different operating temperatures and cathode pressures is investigated experimentally. Polarization curves and EIS spectra are measured to characterize the performance of the PEMWE. A distribution of relaxation times-based approach is proposed to quantify the internal polarization processes. This enables analysis of the influence of operating temperature and cathode pressure on the performance of the PEMWE through the decomposed polarization resistances. The main findings of this study are as follows:

- Four internal polarization processes are identified from the EIS spectra of the studied PEMWE stack, including proton transport in the ionomer of the catalyst layer (200-2000 Hz), charge transfer during OER (1.5-280 Hz) and HER (30-230 Hz), and mass transport (0.2-7 Hz).

Table A.1: Physical parameters of the considered PEM fuel cell [48].

Parameter description	Unit	Value
Thickness of membrane	μm	15
Thickness of gas diffusion layer	μm	220± 20
Thickness of catalyst layer	μm	6-8
Anode platinum loading	mg.cm^{-2}	JM Pt/C 0.1
Cathode platinum loading	mg.cm^{-2}	JM Pt/C 0.4
Cell active area	cm^2	25

- The HFR (contributes 79.4%) and charge transfer processes (16.4%) are the dominant factors for determining the overall performance of the PEMWE. By comparing with the fuel cell DRT results, the weights of different polarization processes are further clarified.
- The performance of the PEMWE is enhanced with increasing temperature. The decomposed polarization resistances show that the improvement is mainly due to the enhanced conductivity of cell components at higher temperatures.
- In the lower and middle current range, the performance of the PEMWE decreases with increasing pressure due to the increased input energy required to initiate the water electrolysis process. However, in the high current range, the performance of the PEMWE at 3 bar and 5 bar is below that of 1 bar. The internal polarization processes are enhanced with increasing pressure, thus causing a slight decrease in stack voltage.

Future work will be done to investigate the durability of the PEMWE under different operating conditions, with a focus on evaluating performance heterogeneity. The tests under extreme conditions will also be studied to ensure the completeness of the proposed studies. The in-plane performance heterogeneity in each cell and heterogeneity across different cells will be characterized. Attention will be paid to repeating the EIS measurement to ensure the accuracy of the obtained impedance spectra. The proposed DRT-based method can be applied to quantify the variation trend of key polarization processes during the durability test. We may further quantify their contribution to degradation to identify the root causes of degradation. The influence of temperature, pressure, and other factors such as water flow rate on the degradation heterogeneity of the PEMWE will be quantified.

Acknowledgment

This work has been supported by France 2030/PEPR Hydrogène décarboné/Project DuraSyS-PAC managed by the French Research Agency (Reference ANR-22-PEHY-0002), ANR Chaire de Professeur Junior project (ANR-22-CPJ1-0074-01), the EIPHI Graduate School (contract ANR-17-EURE-0002) and the Region Bourgogne Franche-Comté.

Appendix A. Physical parameters of the PEM fuel cell

The physical parameters of the considered PEM fuel cell are summarized in Table A.1. The graphite bipolar plate with a serpentine flow field is used in the test.

References

[1] T. T. Le, P. Sharma, B. J. Bora, V. D. Tran, T. H. Truong, H. C. Le, P. Q. P. Nguyen, Fueling the future: A comprehensive review of hydrogen energy systems and their challenges, International Journal of Hydrogen Energy 54 (2024) 791–816.

[2] J. Zuo, N. Y. Steiner, Z. Li, D. Hissel, Health management review for fuel cells: Focus on action phase, Renewable and Sustainable Energy Reviews 201 (2024) 114613.

[3] Y. Wang, Y. Pang, H. Xu, A. Martinez, K. S. Chen, PEM fuel cell and electrolysis cell technologies and hydrogen infrastructure development–a review, Energy & Environmental Science 15 (2022) 2288–2328.

[4] M. Chatenet, B. G. Pollet, D. R. Dekel, F. Dionigi, J. Deseure, P. Millet, R. D. Braatz, M. Z. Bazant, M. Eikerling, I. Staffell, et al., Water electrolysis: from textbook knowledge to the latest scientific strategies and industrial developments, Chemical Society Reviews 51 (2022) 4583–4762.
[5] S. S. Kumar, V. Himabindu, Hydrogen production by PEM water electrolysis–A review, Materials Science for Energy Technologies 2 (2019) 442–454.
[6] S. Grigoriev, V. Fateev, D. Bessarabov, P. Millet, Current status, research trends, and challenges in water electrolysis science and technology, International Journal of Hydrogen Energy 45 (2020) 26036–26058.
[7] M. N. I. Salehmin, T. Husaini, J. Goh, A. B. Sulong, High-pressure pem water electrolyser: A review on challenges and mitigation strategies towards green and low-cost hydrogen production, Energy Conversion and Management 268 (2022) 115985.
[8] H.-O. Lee, J. Yesuraj, K. Kim, Parametric study to optimize proton exchange membrane electrolyzer cells, Applied Energy 314 (2022) 118928.
[9] Y. Zhu, Y. Zhang, S. Bin, Z. Chen, F. Zhang, S. Gong, Y. Xia, X. Duan, Effects of key design and operating parameters on the performance of the PEM water electrolysis for hydrogen production, Renewable Energy 235 (2024) 121290.
[10] A. Bazarah, E. H. Majlan, T. Husaini, A. Zainoodin, I. Alshami, J. Goh, M. S. Masdar, Factors influencing the performance and durability of polymer electrolyte membrane water electrolyzer: A review, International Journal of Hydrogen Energy 47 (2022) 35976–35989.
[11] J. Chen, S. Wang, Y. Sun, C. Zhang, H. Lv, Multi-dimensional performance evaluation and energy analysis of proton exchange membrane water electrolyzer, Applied Energy 377 (2025) 124457.
[12] H. Li, A. Inada, T. Fujigaya, H. Nakajima, K. Sasaki, K. Ito, Effects of operating conditions on performance of high-temperature polymer electrolyte water electrolyzer, Journal of Power Sources 318 (2016) 192–199.
[13] Ö. F. Selamet, M. C. Acar, M. D. Mat, Y. Kaplan, Effects of operating parameters on the performance of a high-pressure proton exchange membrane electrolyzer, International Journal of Energy Research 37 (2013) 457–467.
[14] S. Yuan, C. Zhao, X. Cai, L. An, S. Shen, X. Yan, J. Zhang, Bubble evolution and transport in PEM water electrolysis: Mechanism, impact, and management, Progress in Energy and Combustion Science 96 (2023) 101075.
[15] E. Afshari, S. Khodabakhsh, N. Jahantigh, S. Toghyani, Performance assessment of gas crossover phenomenon and water transport mechanism in high pressure PEM electrolyzer, International Journal of Hydrogen Energy 46 (2021) 11029–11040.
[16] G. Correa, P. Marocco, P. Muñoz, T. Falagüerra, D. Ferrero, M. Santarelli, Pressurized PEM water electrolysis: Dynamic modelling focusing on the cathode side, International Journal of Hydrogen Energy 47 (2022) 4315–4327.
[17] A. Martin, P. Trinke, M. Stähler, A. Stähler, F. Scheepers, B. Bensmann, M. Carmo, W. Lehnert, R. Hanke-Rauschenbach, The effect of cell compression and cathode pressure on hydrogen crossover in PEM water electrolysis, Journal of the Electrochemical Society 169 (2022) 014502.
[18] N. Li, S. S. Araya, X. Cui, S. K. Kær, The effects of cationic impurities on the performance of proton exchange membrane water electrolyzer, Journal of Power Sources 473 (2020) 228617.
[19] S. Wang, J. Zhang, O. Gharbi, V. Vivier, M. Gao, M. E. Orazem, Electrochemical impedance spectroscopy, Nature Reviews Methods Primers 1 (2021) 41.
[20] M. Suermann, B. Bensmann, R. Hanke-Rauschenbach, Degradation of proton exchange membrane (PEM) water electrolysis cells: looking beyond the cell voltage increase, Journal of The Electrochemical Society 166 (2019) F645.
[21] Z. Tang, Q.-A. Huang, Y.-J. Wang, F. Zhang, W. Li, A. Li, L. Zhang, J. Zhang, Recent progress in the use of electrochemical impedance spectroscopy for the measurement, monitoring, diagnosis and optimization of proton exchange membrane fuel cell performance, Journal of Power Sources 468 (2020) 228361.
[22] D. Li, R. Qi, L.-Z. Zhang, Electrochemical impedance spectroscopy analysis of V–I characteristics and a fast prediction model for PEM-based electrolytic air dehumidification, International Journal of Hydrogen Energy 44 (2019) 19533–19546.
[23] J. C. Garcia-Navarro, M. Schulze, K. A. Friedrich, Measuring and modeling mass transport losses in proton exchange membrane water electrolyzers using electrochemical impedance spectroscopy, Journal of Power Sources 431 (2019) 189–204.
[24] I. Franzetti, A. Pushkarev, A.-L. Chan, T. Smolinka, Parasitic Effects in Impedance Spectrum of PEM Water Electrolysis Cells: Case Study of High-Frequency Inductive Effects, Energy Technology 11 (2023) 2300375.
[25] F. Ciucci, Modeling electrochemical impedance spectroscopy, Current Opinion in Electrochemistry 13 (2019) 132–139.
[26] H. Lu, J. Chen, C. Yan, H. Liu, On-line fault diagnosis for proton exchange membrane fuel cells based on a fast electrochemical impedance spectroscopy measurement, Journal of Power Sources 430 (2019) 233–243.
[27] W. Aït-Idir, P. Wu, R. Sgarbi, Q. Labarde, S. Touhami, M. Daoudi, J.-C. Perrin, J. Dillet, C. Marty, F. Micoud, et al., Oxygen diffusion impedance in proton exchange membrane fuel cells–insights into electrochemical impedance spectra and equivalent electrical circuit modeling, Electrochimica Acta 472 (2023) 143430.
[28] C. Plank, T. Rüther, L. Jahn, M. Schamel, J. P. Schmidt, F. Ciucci, M. A. Danzer, A review on the distribution of relaxation times analysis: A powerful tool for process identification of electrochemical systems, Journal of Power Sources (2023) 233845.
[29] Y. Lu, C.-Z. Zhao, J.-Q. Huang, Q. Zhang, The timescale identification decoupling complicated kinetic processes in lithium batteries, Joule 6 (2022) 1172–1198.
[30] Q. Zhang, D. Wang, E. Schaltz, D.-I. Stroe, A. Gismero, B. Yang, Degradation mechanism analysis and state-of-health estimation for lithium-ion batteries based on distribution of relaxation times, Journal of Energy Storage 55 (2022) 105386.
[31] R. He, Y. He, W. Xie, B. Guo, S. Yang, Comparative analysis for commercial li-ion batteries degradation using the distribution of relaxation time method based on electrochemical impedance spectroscopy, Energy 263 (2023) 125972.
[32] H. Yuan, H. Dai, P. Ming, X. Wang, X. Wei, Quantitative analysis of internal polarization dynamics for polymer electrolyte membrane fuel cell by distribution of relaxation times of impedance, Applied Energy 303 (2021) 117640.
[33] M. Heinzmann, A. Weber, E. Ivers-Tiffée, Impedance modelling of porous electrode structures in polymer electrolyte membrane fuel cells, Journal of Power Sources 444 (2019) 227279.
[34] M. Heinzmann, A. Weber, Impedance based performance model for polymer electrolyte membrane fuel cells, Journal of Power Sources 558 (2023) 232540.

[35] Y. Ao, Z. Li, S. Laghrouche, D. Depernet, D. Candusso, K. Zhao, Stack-level diagnosis of proton exchange membrane fuel cell by the distribution of relaxation times analysis of electrochemical impedance spectroscopy, Journal of Power Sources 603 (2024) 234420.
[36] J. Zuo, N. Y. Steiner, Z. Li, D. Hissel, Degradation root cause analysis of PEM fuel cells using distribution of relaxation times, Applied Energy 378 (2025) 124762.
[37] J. Kwon, P. Choi, S. Jo, H. Oh, K.-Y. Cho, Y.-K. Lee, S. Kim, K. Eom, Identification of electrode degradation by carbon corrosion in polymer electrolyte membrane fuel cells using the distribution of relaxation time analysis, Electrochimica Acta 414 (2022) 140219.
[38] Y. Li, Y. Jiang, J. Dang, X. Deng, B. Liu, J. Ma, F. Yang, M. Ouyang, X. Shen, Application of distribution of relaxation times method in polymer electrolyte membrane water electrolyzer, Chemical Engineering Journal 451 (2023) 138327.
[39] B. S. Batalla, J. Bachmann, C. Weidlich, Investigation of the degradation of proton exchange membrane water electrolysis cells using electrochemical impedance spectroscopy with distribution of relaxation times analysis, Electrochimica Acta 473 (2024) 143492.
[40] A. M. Dhirde, N. V. Dale, H. Salehfar, M. D. Mann, T.-H. Han, Equivalent electric circuit modeling and performance analysis of a PEM fuel cell stack using impedance spectroscopy, IEEE transactions on energy conversion 25 (2010) 778–786.
[41] M. Schönleber, D. Klotz, E. Ivers-Tiffée, A method for improving the robustness of linear Kramers-Kronig validity tests, Electrochimica Acta 131 (2014) 20–27.
[42] H. Li, Z. Lyu, M. Han, Robust and fast estimation of equivalent circuit model from noisy electrochemical impedance spectra, Electrochimica Acta 422 (2022) 140474.
[43] T. H. Wan, M. Saccoccio, C. Chen, F. Ciucci, Influence of the discretization methods on the distribution of relaxation times deconvolution: implementing radial basis functions with DRTtools, Electrochimica Acta 184 (2015) 483–499.
[44] J. J. Giner-Sanz, E. Ortega, V. Pérez-Herranz, Mechanistic equivalent circuit modelling of a commercial polymer electrolyte membrane fuel cell, Journal of Power Sources 379 (2018) 328–337.
[45] A. Maradesa, B. Py, J. Huang, Y. Lu, P. Iurilli, A. Mrozinski, H. M. Law, Y. Wang, Z. Wang, J. Li, et al., Advancing electrochemical impedance analysis through innovations in the distribution of relaxation times method, Joule (2024).
[46] Z. Lyu, H. Li, M. Han, Z. Sun, K. Sun, Performance degradation analysis of solid oxide fuel cells using dynamic electrochemical impedance spectroscopy, Journal of Power Sources 538 (2022) 231569.
[47] J. Zuo, H. Lv, D. Zhou, Q. Xue, L. Jin, W. Zhou, D. Yang, C. Zhang, Long-term dynamic durability test datasets for single proton exchange membrane fuel cell, Data in Brief 35 (2021) 106775.
[48] J. Zuo, H. Lv, D. Zhou, Q. Xue, L. Jin, W. Zhou, D. Yang, C. Zhang, Deep learning based prognostic framework towards proton exchange membrane fuel cell for automotive application, Applied Energy 281 (2021) 115937.
[49] M. Kaya, N. Demir, Numerical investigation of PEM water electrolysis performance for different oxygen evolution electrocatalysts, Fuel Cells 17 (2017) 37–47.
[50] Z. Kang, S. M. Alia, J. L. Young, G. Bender, Effects of various parameters of different porous transport layers in proton exchange membrane water electrolysis, Electrochimica Acta 354 (2020) 136641.
[51] N. Hensle, D. Brinker, S. Metz, T. Smolinka, A. Weber, On the role of inductive loops at low frequencies in PEM electrolysis, Electrochemistry Communications 155 (2023) 107585.
[52] T. Lickert, M. L. Kiermaier, K. Bromberger, J. Ghinaiya, S. Metz, A. Fallisch, T. Smolinka, On the influence of the anodic porous transport layer on PEM electrolysis performance at high current densities, International Journal of Hydrogen Energy 45 (2020) 6047–6058.
[53] M. Suermann, T. J. Schmidt, F. N. Büchi, Cell performance determining parameters in high pressure water electrolysis, Electrochimica Acta 211 (2016) 989–997.